REBOund: Untethered Origami Jumping Robot with Controllable Jump Height

Jaimie Carlson, Jason Friedman, Christopher Kim, Cynthia Sung

Abstract— **Origami robots are well-suited for jumping maneuvers because of their light weight and ability to incorporate actuation and control strategies directly into the robot body. However, existing origami robots often model fold patterns as rigidly foldable and fail to take advantage of deformation in an origami sheet for potential energy storage. In this paper, we consider a parametric origami tessellation, the Reconfigurable Expanding Bistable Origami (REBO) pattern, which leverages face deformations to act as a nonlinear spring. We present a pseudo-rigid-body model for the REBO for computing its energy stored when compressed to a given displacement and compare that model to experimental measurements taken on a mechanical testing system. This stored potential energy, when released quickly, can cause the pattern to jump. Using our model and experimental data, we design and fabricate a jumping robot, REBOund, that uses the spring-like REBO pattern as its body. Four lightweight servo motors with custom release mechanisms allow for quick compression and release of the origami pattern, allowing the fold pattern to jump over its own height even when carrying 5 times its own weight in electronics and power. We further demonstrate that small geometric changes to the pattern allow us to change the jump height without changing the actuation or control mechanism.**

I. INTRODUCTION

In nature, jumping allows organisms to escape dangerous situations and surpass obstacles higher than their body height. These maneuvers can be very important for robots placed in uncontrolled or potentially hazardous environments. Recent jumping [1], [2] and hopping [3], [4] robots have demonstrated that it is possible to jump several meters high [5] using a variety of mechanisms ranging from snail cams [6] to snap-through buckling [2] to controlled explosions [7]. Often, these mechanisms are carefully optimized [8] to attain a particular (usually maximum) jump height within actuation constraints. Part of this optimization includes an effort to minimize the weight of infrastructure that is required to keep the mechanism together but serves little other functional purpose. These optimizations often sacrifice additional complexity, such as precise control of jump height or jump angle [1], [6], [9]. When jumping height can be controlled [10], [11], the mechanisms require precise characterization and actuation strategies.

Simultaneously, origami-inspired robots [12] have emerged as a method for reducing weight [13] and fully integrating electronics [14] without sacrificing kinematic complexity [15]. Demonstrations for a wide variety of locomotion modes, including walking [16], swimming [17], worm-like locomotion [18], gliding [19], and flight [20], indicate that origami robots may be suited to a similar range of movements as robots fabricated through more traditional means. However, because these robots are assembled from thin films, which bend and deform, existing origami robots have been limited to applications requiring small robots carrying small loads.

Our main insight is that existing approaches to origami design fail to leverage the a sheet's ability to deform to create stronger and more robust structures. The majority of origami robots use a "rigid origami" model [21], which assumes that faces are perfectly rigid and folds are rotational hinges, often modeled as torsion springs [15]. When using this model, all forces required for motion come from resistance in the folds themselves, and the rigid faces are assumed to maintain kinematic constraints (e.g., locking zero-degree-of-freedom components) perfectly. Existing origami jumping robots therefore must add additional springs [8] or carefully chosen materials [14], [22] at select folds to store the potential energy required to jump, when instead they could store potential energy into the fold pattern itself.

In this paper, we explore an origami design's non-rigid deformation and use these insights to tune the mechanics of an origami pattern for jumping behavior. Because origami designs are folded from flexible sheets and not rigid panels, the pattern can store and release potential strain energy, and the body of the robot can serve a dual purpose as both frame and jumping mechanism. By designing kinematic constraints into a pattern, we control the amount of strain energy stored in the robot's body, allowing us to tune the potential energy and thus the jump height through geometry changes, and simplifying the actuation and control strategy.

Our work leverages the Reconfigurable Expanding Bistable Origami (REBO) pattern [23], [24]. This is a bistable origami pattern that, when folded, snaps between compressed and expanded states. In contrast to our previous study, which focused on the design geometry, we characterize its spring-like behavior. Our contributions include:

- REBOund, an untethered origami jumping robot with tunable jump height based on geometric parameters;
- an experimentally-verified pseudo-rigid-body model that captures the effect of geometry on its force-displacement relationship and potential energy storage;
- a strategy for manipulating fold pattern geometry for jump height control; and
- demonstrations of REBOund robots with different parameters and the ability to switch between them to

The authors are with the General Robotics, Automation, Sensing & Perception (GRASP) Lab at the University of Pennsylvania, Philadelphia, PA, USA Emails: jaimiec@alumni.upenn.edu, {jasonf27, cyoonjae, crsung}@seas.upenn.edu. Support for this project has been provided in part by NSF Grant No. 1138847. We thank Dr. Kevin Turner, Saurya Vankayalapati, and Joanna Wang for assistance on the mechanical testing, and Deyuan Chen, Neera Raychaudhuri, and Dr. James Pikul for helpful discussions.

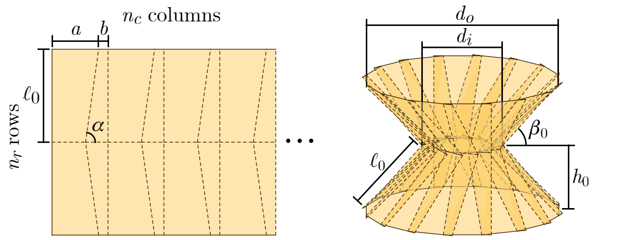

(a) Fold Pattern (b) Folded State

Fig. 1. REBO pattern with parameters indicated. Changes to any of the parameters on the fold pattern (a) affect the geometry of the folded state (b). Solid lines indicate the paper boundary, and dashed lines indicate folds.

achieve jump heights of 97.4 mm and 123.4 mm.

Our results demonstrate how modeling the compliance of an origami pattern in addition to its kinematics can produce more integrated design and control strategies.

The outline of this paper is as follows. Section II presents the REBO pattern and our mechanics model. Section III contains our experimental characterization. Section IV details our untethered REBOund robot design and strategy for geometrically controlled jump height. Section V describes our experimental results. Section VI concludes with a discussion of our results and future work.

II. REBO Origami Pattern

A. Fold Pattern Parameterization

The Reconfigurable Expanding Bistable Origami (REBO) pattern [23] used as the basis of our study is an $n_r \times n_c$ origami tessellation of rectangular units (Fig. 1). Each unit of the tessellation contains two vertical and two horizontal creases on the boundary, and a diagonal crease at an angle α on the interior. The vertical creases fold to an angle of π, while the horizontal folds fold to angle of $\pm 2\beta_0$, depicted in Fig. 1(b), which is dependent on the angle α. As a result, each row of the pattern folds into a right frustum with n_c sides at an angle β_0 from horizontal, producing a folded state with a final height h. The variables d_o and d_i denote the outer and inner diameters of the REBO, respectively. The exact relationship between the fold pattern parameters n_c, n_r, a, b, ℓ_0, and α and the folded state parameters d_o, d_i, h_0, and β_0 is outlined in [23]. Most importantly, decreasing α increases the slant angle β_0 and the layer height h_0. Similarly, increasing the unit length ℓ_0 also increases h_0.

We use one layer (2 rows) of the tessellation for characterization and design. Under rigid origami assumptions, each layer of the REBO would be theoretically locked. The pattern experiences no face deformation in 2 configurations: either expanded as stacked frusta (shown in Fig. 1(b)) or compressed into nested frusta (when the horizontal creases fold to $\pm\pi$ and $h \rightarrow -h_0$). Transitioning between the two states requires the faces to deform through an alternate injection and release of strain potential energy in the pattern and resulting in snap-through between states.

B. Mechanics Model

To predict the strain energy stored in the pattern during compression and expansion, we use the pseudo-rigid-body model [25]–[27] depicted in Fig. 2. Because the REBO is rotationally symmetric, we analyze a planar slice.

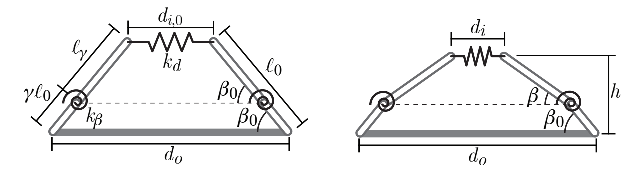

(a) Expanded (b) Compressed

Fig. 2. We model the REBO pattern using a pseudo-rigid-body model with a linear spring representing the inner diameter constraint. The faces are modeled as 2 rigid links connected by a torsion spring.

Due to the thinness of the folded material, the faces of the REBO tend to bend rather than compress as the REBO transitions between states. We therefore approximate the faces as two rigid links connected by a torsional spring. The placement of the torsional spring along the face with length ℓ_0 depends on its geometry according to a parameter $\gamma \in [0, 0.5]$ [26]. The torsional spring has spring constant k_β and rest angle β_0. As the REBO is compressed or expanded to a height h, its shape deforms as in Fig. 2(b). The bottom portion of each face maintains the slope angle β_0 of the undeformed REBO, and the top portion of the face bends to accommodate. The rest angle β_0 can be determined theoretically using the equations in [23] or measured directly from the fabricated pattern.

The pleats in the fold pattern allow for sliding between the faces, meaning that the inner diameter of the folded REBO is not fully constrained. Experimentally, this inner diameter has been observed to change by up to 6% when the REBO compresses. To model changes in the inner diameter, we use a linear spring with spring constant k_d and rest length $d_{i,0}$, where $d_{i,0}$ can be computed as

$$d_{i,0} = d_o - 2\ell_0 \cos\beta_0 \tag{1}$$

The REBO's height h, slant angle β, and inner diameter d_i are coupled by

$$\ell_\gamma = (1-\gamma)\ell_0 \tag{2}$$

$$h = \gamma\ell_0 \sin\beta_0 + \ell_\gamma \sin\beta \tag{3}$$

$$d_i = d_o - 2\left(\gamma\ell_0 \cos\beta_0 + \ell_\gamma \cos\beta\right) \tag{4}$$

The potential strain energy U stored in the REBO is

$$U = U_\beta + U_d \tag{5}$$

$$U_\beta = \frac{1}{2}k_\beta(\beta - \beta_0)^2 \tag{6}$$

$$U_d = \frac{1}{2}k_d(d_i - d_{i,0})^2 \tag{7}$$

The vertical reaction force F produced by the REBO is

$$F = \frac{dU}{dh} = F_\beta + F_d \tag{8}$$

where combining with Eqs. (3), (4), (6), and (7) yields

$$F_\beta = \frac{dU_\beta}{dh} = \frac{k_\beta}{\ell_\gamma}(\beta - \beta_0)\sec\beta \tag{9}$$

$$F_d = \frac{dU_d}{dh} = -4k_d\ell_\gamma(\cos\beta - \cos\beta_0)\tan\beta \tag{10}$$

TABLE I
PARAMETERS TESTED ($a = 15$ MM, $b = 3$ MM, $n_c = 16$)

$\alpha = 80°$	$\ell_0 = \{20$ mm, 25 mm, 27.5 mm, 30 mm, 32.5 mm, 35 mm, 40 mm$\}$
$\ell_0 = 30$ mm	$\alpha = \{84°, 83°, 82°, 81°, 80.5°, 80°, 79.5°, 79°, 78°\}$

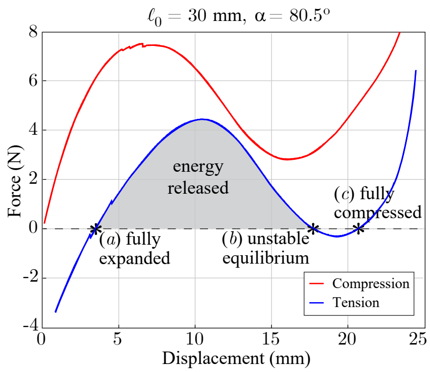

Fig. 3. (a) One trial of measured force vs. displacement for a REBO with parameters $\ell_0 = 30$ mm, $\alpha = 80.5°$. Positive values for force indicate compressive direction (down), and negative values indicate tension (up). There are two stable equilibria and one unstable equilibrium. The area under the tension curve between states (a) and (b) is the energy released when jumping.

III. MECHANICS MEASUREMENTS

We took experimental measurements over a parameter sweep across 15 REBO samples with varying ℓ_0 and α values (ref. TABLE I). The other fold pattern parameters were kept constant at $a = 15$ mm, $b = 3$ mm, and $n_c = 16$ for all samples. We included two samples ($\ell_0 = 30$ mm, $\alpha = 78°$ and $\ell_0 = 40$ mm, $\alpha = 80°$) that are theoretically infeasible due to self-collision in the folded state, but are practically foldable. All REBOs had top and bottom rows of $a = 15$ mm, $b = 3$ mm, $n_c = 16$, $\alpha = 90°$, and $h = 40$ mm for simpler mounting to measurement equipment. The samples were fabricated from 0.127 mm thick PET film using a Universal Laser Systems PLS4.75 laser cutter. Folds were perforated at 35 pulses per inch.

A. Force-Displacement Curves

To verify our pseudo-rigid-body model and predict jump height, we ran compression and tension tests for all samples using an MTS Criterion Model 43 uniaxial testing machine with 50 N load cell. The samples were attached to the system using 3D printed PLA caps. Alternating compression and tension tests were run on each REBO sample between its fully extended and fully compressed states. For each sample, three tests were run at 10 mm/min.

Figure 3 shows the force vs. displacement for one compression and tension trial for a REBO with $\ell_0 = 30$ mm, $\alpha = 80.5°$. These nonlinear curves are typical of all of the samples. Hysteresis can be observed, as the compression and tension curves are not identical due to plastic deformation in the folds as the REBO compresses. Since we are interested in the energy released when the REBO decompresses, we analyze the tension curves.

We fit the model parameters k_β, k_d, and γ to the experimental tension curves using MATLAB's `fmincon` with interior-point algorithm. The experimental measurements were shifted so that the displacement was zero at the first stable equilibrium. Parameters were computed to minimize the sum of squared error between predicted and measured force at each displacement. One fit was performed for each sample using all three sets of experimental data. Figure 4 shows the resulting fits for three of these samples. The model matches the general shape of the experimental force-displacement curves. For most of the samples, such as Fig. 4(b), the pseudo-rigid-body model is a good fit. However, when α was high (e.g., Fig. 4(a)), the sample tended to buckle in the bottom half, and the fit was not as good. For infeasible samples such as Fig. 4(c), the model was unable to predict the REBO's behavior. This is not unexpected, since this model theoretically cannot exist.

B. Jump Height

The experimental measurements and the model were used to predict jump height. Referring to the tension curve in Fig. 3, the REBO experiences two stable equilibrium states (expanded state a and fully compressed state c), and one unstable equilibrium state b in the middle. To calculate energy stored in the REBO for a jump, we assume that the REBO has been perturbed from c to b. (When the REBO did not experience snap-through, then the local minimum of force was used as the state b. For the pseudo-rigid-body model, if there was no local minimum of force, the average b for the corresponding experimental curves was used.) Then, it moves on its own from the unstable equilibrium b to the stable equilibrium a along the tension force-displacement curve $F_{tension}$, releasing stored jumping energy U_{jump} and jumping to a height z

$$U_{jump} = \int_a^b F_{tension}(h)dh \tag{11}$$

$$z = \frac{U_{jump}}{mg} \tag{12}$$

where m is REBO mass and g is gravitational acceleration.

Figure 5 compares energy storage predictions between experimental tension curves and curves from the pseudo-rigid-body model. Both models agree on the general trends.

We also compared these jump height predictions against samples tracked in an OptiTrack motion capture system. Each REBO was manually compressed to just past its unstable equilibrium and released. A 21.1 g PLA cap was added to the top of the sample to simulate mass of motors and control electronics. Each sample was tested over a total of 10 trials. Figure 6 shows the comparison between the motion capture data (MC), jump heights predicted using the pseudo-rigid-body model (PRBM), and jump heights predicted from the tension measurements (TM).

It is clear that both parameters ℓ_0 and α have an effect on the jump height achievable by the REBO. In particular, increasing ℓ_0 decreases the jump height approximately linearly. Increasing α tends to increase jump height until

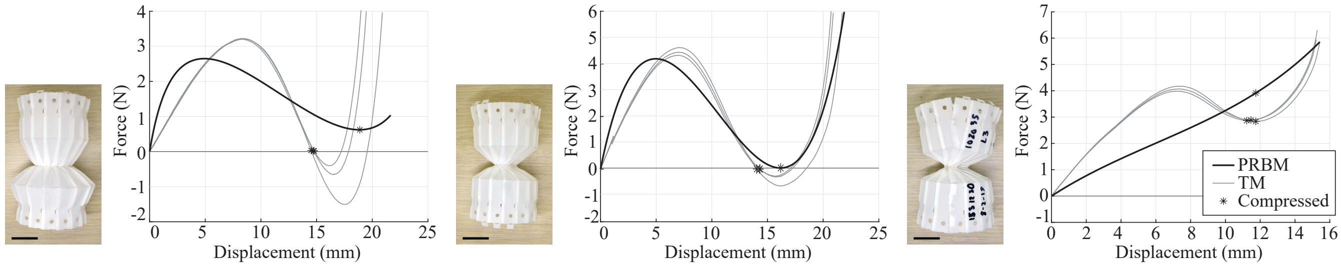

(a) $\ell_0 = 30$ mm, $\alpha = 84°$ (b) $\ell_0 = 30$ mm, $\alpha = 80.5°$ (c) $\ell_0 = 30$ mm, $\alpha = 78°$

Fig. 4. REBO samples with measured force-displacement curves and fits of the pseudo-rigid-body model. The black scale bar is 2 cm. Stars on the plots indicate the unstable equilibrium or a local minimum of force. These were the displacements used to predict jumping energy. (a) For high α values, buckling occurs, but the model is able to match the general shape of the curve. (b) The spring model provides a good prediction for most middle ℓ_0 and α values. (c) The pattern is theoretically infeasible with a negative β (which was clipped to a very small β in the model to avoid physically meaningless solutions). This prevented the large change in d_i which could lead to an accurate bistable curve, so the model does not match.

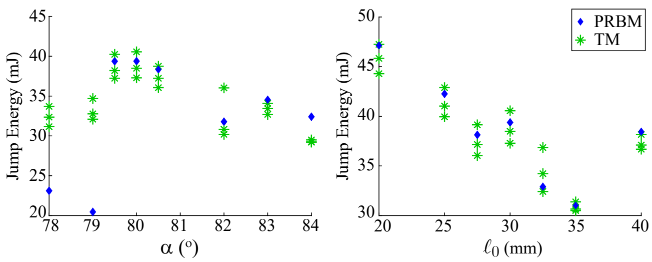

(a) $\ell_0 = 30$ mm, changing α (b) $\alpha = 80°$, changing ℓ_0

Fig. 5. Jump energy comparisons between experimental tension measurements (TM) and the pseudo-rigid-body model (PRBM). (a) Peak energy storage increases, then decreases, with α. (b) Peak energy storage decreases with l_0.

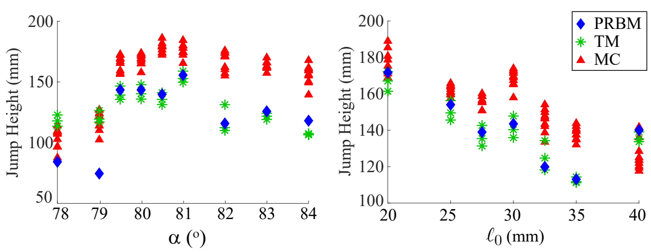

(a) $\ell_0 = 30$ mm, changing α (b) $\alpha = 80°$, changing ℓ_0

Fig. 6. Jump height comparison between motion capture data (MC), predictions from experimental tension curve energy calculations (TM), and the pseudo-rigid-body model (PRBM). (a) Jump height increases, then decreases, with α. (b) Jump height decreases with ℓ_0.

some maximum-height value at approximately $\alpha = 81°$ (for $\ell_0 = 30$ mm), after which jump height starts to decrease. Theoretically, we should expect that as α increases, β_0 also increases, the distance over which the REBO is compressed increases, and thus jump height increases. Practically, this was not the case. We suspect that the difference lies in how the REBO compresses when it has large α. Figure 4 shows that for large α values, the bottom of the REBO buckles, thus producing a lower effective α and slope angle β_0. As a comparison, TABLE II lists the theoretical and measured slope angles β_0 for each of the samples in Fig. 4. The $\alpha = 84°$ REBO actually has a β_0 value close to that of the $\alpha = 80.5°$ REBO, thus resulting in similar energy storage and jump height. This was true for all REBOs with $\alpha \geq 83°$.

TABLE II

THEORETICAL VS MEASURED β_0

ℓ_0 (mm)	α (deg.)	$\beta_{0,th}$ (deg.)	$\beta_{0,meas}$ (deg.)
30	84	58.10	35.68
30	80.5	32.72	30.51
30	78	N/A	21.51

The predictions of the experimental tension measurements and of the pseudo-rigid-body model agree very well with each other, and with the motion-capture jump height data's overall trends. Except for the outliers at low $\alpha = 78°$ and $79°$ (which are not theoretically feasible) and at $\alpha = 84°$ (where there was some additional buckling), the pseudo-rigid-body model force-displacement curves tended to resemble Fig. 4(b) in fit quality, and their predicted jump heights were always within 1 cm of the average tension-measurement jump height.

Both the pseudo-rigid-body-model and the tension measurements underpredict experimentally measured jump height. This may be due to a viscoelastic effect: we observed that REBOs compressed for a longer time do not jump as high. Energy which might be dissipated during a slow tension test may be available during a quick jumping release.

IV. State-Switching REBOund Jumping Robot

Based on our experimental measurements, it is clear that slight variations in ℓ_0 and α can have large effects on the jumping behavior of the REBO design. We can therefore manipulate the design parameters of the REBO fold pattern to give us a desired jump height, even with a very simple controller. To demonstrate this concept, we designed and built a jumping robot (Fig. 7) using the REBO pattern as a body. The pattern contains two different "states" which can be activated based on the desired jump height.

A. Fold Pattern Parameters Embedding Two Jump Heights

We observe that the jumping height of the REBO pattern can be manipulated either by changing ℓ_0 or by changing α. We therefore created a state-switching REBO pattern (Fig. 7(b)) embedding two designs with the same unit length ℓ_0 but different α values. Due to the structure of the REBO tessellation, the majority of the two patterns is the same,

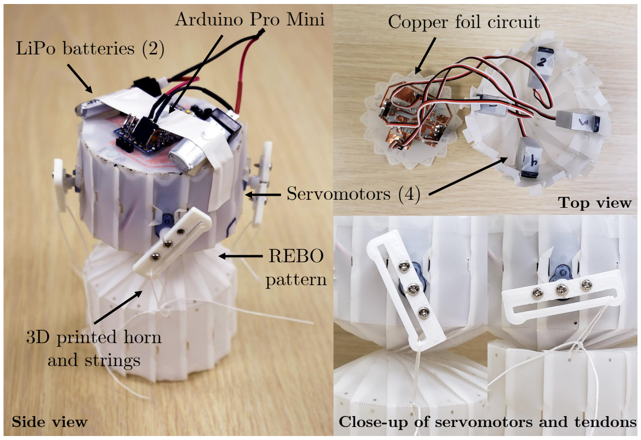

(a) Assembled Robot

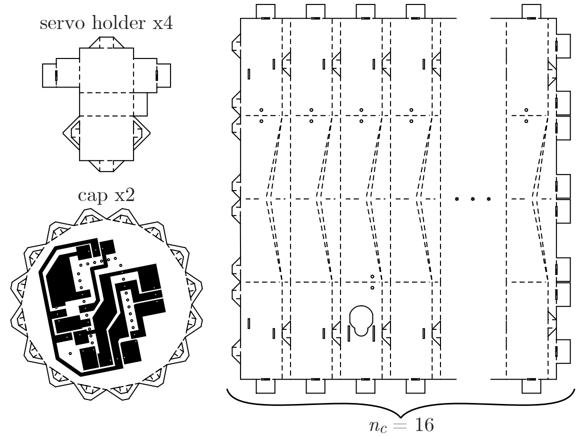

(b) State-Switching Pattern

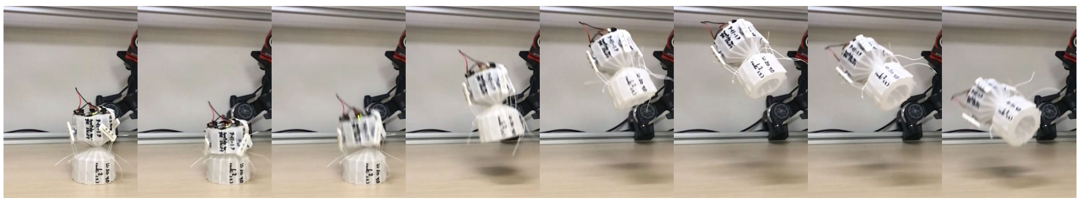

0 ms | 125 ms | 137.5 ms | 187.5 ms | 250 ms | 312.5 ms | 375 ms | 437.5 ms

(c) Snapshots

Fig. 7. Final state-switching REBOund design. (a) Assembled robot. (b) Full fold pattern for REBOund body, including 4 servo holders, 2 caps (circuit layout on the top cap), and body with ($\ell_0 = 30$ mm, $\alpha = 82°$) and ($\ell_0 = 30$ mm, $\alpha = 79°$) patterns embedded. (c) Snapshots of REBOund actuation over time.

with the only major difference being the introduction of two diagonal folds, rather than the original single fold, at the two desired α values.

Note that in the folded state, it is possible for only one of these diagonal folds to be active at any one time, and that if one is folded, the other must lie flat. The pattern can be switched manually from one state to the other by pulling on the frustum to activate the $\alpha = 82°$ set of folds, or pushing on the frustum to activate the $\alpha = 79°$ set of folds. Interestingly, intermediate states can be activated by activating different folds on each of the different columns of the REBO, although in this case the structure may no longer be rotationally symmetric.

For our experiments, we chose fold pattern parameters $n_c = 16$, $a = 15$ mm, $b = 3$ mm, $\ell_0 = 30$ mm, with $\alpha = 79°$ and $\alpha = 82°$. Holes were added to four sides of the pattern to mount servomotors and tendons. In addition, two caps were fabricated for the top and bottom of the robot to maintain the outer diameter of the robot at d_o.

B. Fabrication

The robot body was cut out of 0.127 mm thick PET film using a PLS4.75 laser cutter. Folds were perforated at 40 pulses per inch. Four servomotors (Turnigy TGY-0025) capable of producing a torque of 0.8 kg-cm each actuate the REBO. The servos were mounted using folded servo holders, which were attached to the REBO body using tabs and slots. Strings connecting the servomotors to holes in the REBO pattern allow the servomotors to compress the robot. The servomotor horns were designed with a P-shaped hole to release strings quickly. They were 3D printed from PLA on a Makerbot 2. The servos were controlled using an Arduino Pro Mini mounted to the top cap. The components were electrically connected via a flexible circuit board cut out of copper foil using a Cameo Silhouette vinyl cutter and adhered to the inside of the top cap. The entire fabrication takes less than 3 hours. Figure 7(a) shows the final result. The robot weighs a total of 38.7 g, with mass breakdown given in TABLE III.

TABLE III
MASS BREAKDOWN OF REBOUND ROBOT

REBOund component	Mass (g)
fold pattern	6.9
servo motors and horns	17.8
electronics	5.2
batteries	8.8
total	38.7

C. Control

Because the jumping height control is embedded into the fold pattern itself, the control strategy for the robot is relatively simple (ref. Fig. 7(a), bottom right). The microcontroller was programmed to set the servomotors to an initial angle of $\theta_0 = 30°$ from vertically downward. At this point, the strings are taut and the REBO is fully expanded. In order to jump (triggered by a push button), all four servomotors rotate $d\theta = 120°$ counterclockwise. The string is pulled, and the REBO is compressed a distance of

$$dh = r_h[\cos\theta_0 - \cos(\theta_0 + d\theta)] \tag{13}$$

TABLE IV

PERFORMANCE OF REBOUND ROBOT VS. HAND-ACTUATED TESTS

REBOund	$\alpha = 79°$	$\alpha = 82°$
# trials	6	6
mean, mm	97.4	123.4
std. dev., mm	8.5	5.4
Hand-actuation		
# trials	10	10
mean, mm	118.5	167.4
std. dev., mm	8.1	7.7

where $r_h = 22$ mm is the radius of the servomotor horn. Once the servomotor horn rotates to point near vertically upward, the strings slip off the inside of the P, snap, and release the REBO to jump. Afterwards, the servomotors return to their initial angle to prepare for a new jump.

The main control challenge is that compressing the REBO creates large internal stresses in the material. When multiple α options are available, the pattern tends to snap into the lower-α state during compression. Thus, in the absence of any internal constraints, the REBOund will default to jumping at the lowest jump height. To prevent this, we 3D-printed a small cylinder to insert at the center of the REBOund that enforces that the inner radius r_i remain at its larger (higher α) value. We currently manually insert this cylinder to change jump height. Future work would include actuating this state change. Note that there is no change to the input control signal sent to the servomotors as a result of the state change.

V. EXPERIMENTAL RESULTS

TABLE IV shows the results of jumping experiments with the state-switching REBOund robot. Data for six jumps was taken for each state of the robot. The $\alpha = 79°$ state resulted in mean jump heights of 97.4 mm, with a standard deviation of 8.5 mm over the 6 trials In comparison, the $\alpha = 82°$ state resulted in mean jump heights of 123.4 mm, with a standard deviation of 5.4 mm. Thus, by changing the angle α by only $3°$, we can change the jump height of the REBOund by over 25 mm (21.1%). Compared to the hand-actuated tests in Section III-B, these robots jumped about 18% to 26% lower. Since, the final mass of the robot was 38.2% higher than that of the hand-actuated sample, the robots actually jumped 1% to 13% higher than expected. This increase in performance can be attributed to the greater synchronicity between the four servomotors than can be achieved by hand.

To understand the impact of the extra folds added to the state-switching REBOund design, we also fabricated a single-state REBOund containing only one set of diagonal folds corresponding to the $\alpha = 79°$ pattern. Measurements over 6 jump tests on this design resulted in a mean jump height of 138 mm, with a standard deviation of 8.4 mm. This seems to indicate that introducing additional folds reduces jump height, even when the folds are not active. This makes sense given that the additional folds are perforated into the material, overall weakening the face and reducing its stiffness. Further investigation is required to fully understand the impact of these additional folds on the REBO mechanics.

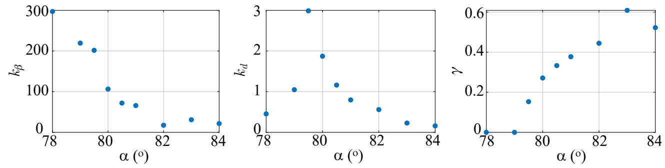

Fig. 8. Values of k_β, k_d, and γ vary with ℓ_0 and α.

VI. DISCUSSION

This paper presents an approach to using and controlling origami compliance for jumping behaviors. We characterized the mechanics of the REBO pattern and its capability for potential energy storage. Using our spring-based pseudo-rigid-body model, we predicted jump height of REBOs with different two-dimensional parameters. We designed an untethered jumping robot, REBOund, which was able to jump up to 123.4 mm and switch between a high- and low-jumping state.

Our results demonstrate that folding can be a tool not only for decreasing weight, as seen in previous robots, but also for actively designing and tuning a robot's bodily compliance. It is important to note that the REBO pattern itself was the source of spring potential energy used in jumping, and that this 6.9 g piece of folded material was capable of lifting over five times its own weight by more than its own height. We did not in this study optimize the electronics and actuation strategy, instead using off-the-shelf servomotors and microcontroller boards. Integrating computation and actuation directly into the REBO pattern itself will substantially improve jumping performance.

Future work includes a deeper understanding of how the REBO's geometric parameters can be used to predict the parameters of our pseudo-rigid-body model. Figure 8 shows that experimentally fit values of k_β, k_d, and γ depend strongly on α. The same is true of changes with respect to ℓ_0. Understanding the nature of that dependency will strengthen our ability to precisely design the robot's jumping behavior.

Furthermore, this design lends itself to directional jumping. During experiments, we noticed that when the motors were not synchronized, the release strings snapped at different times, and the robot tended to jump at an angle in the direction opposite the string that snapped first. Intentionally actuating the motors at different times could allow us to control jump direction, at the possible expense of height.

Finally, while we manually changed the state of the fold pattern in our experiments, we envision a future design where the slant angle β_0 can be actively controlled on-site. Note that in our state switching pattern, the switch between the two states resulted from an angular difference in α of only $3°$, or a shift in vertex location of only 2 mm (out of a tessellation unit side length of 15 mm). This is an in-plane geometry change of 30%. Future work includes investigating methods for embedded, planar, and distributed actuation strategies that will allow us to manipulate the fold pattern for tunable stiffness to control dynamic jumping behaviors at execution time.

References

[1] S. Li and D. Rus, "JelloCube: A continuously jumping robot with soft body," *IEEE/ASME Transactions on Mechatronics*, vol. 24, no. 2, pp. 447–458, 2019.

[2] J.-S. Koh, E. Yang, G.-P. Jung, S.-P. Jung, J. H. Son, S.-I. Lee, P. G. Jablonski, R. J. Wood, H.-Y. Kim, and K.-J. Cho, "Jumping on water: Surface tension–dominated jumping of water striders and robotic insects," *Science*, vol. 349, no. 6247, pp. 517–521, 2015.

[3] D. W. Haldane, J. K. Yim, and R. S. Fearing, "Repetitive extreme-acceleration (14-g) spatial jumping with Salto-1P," *IEEE/RSJ International Conference on Intelligent Robots and Systems*, 2017.

[4] U. Scarfogliero, C. Stefanini, and P. Dario, "Design and development of the long-jumping "Grillo" mini robot," *IEEE International Conference on Robotics and Automation*, pp. 467–472, 2007.

[5] M. A. Woodward and M. Sitti, "Multimo-bat: A biologically inspired integrated jumping–gliding robot," *The International Journal of Robotics Research*, vol. 33, no. 12, pp. 1511–1529, 2014.

[6] U. Scarfogliero, C. Stefanini, and P. Dario, "A bioinspired concept for high efficiency locomotion in micro robots: the jumping robot Grillo," *IEEE International Conference on Robotics and Automation*, pp. 4037–4042, 2006.

[7] W. A. Churaman, A. P. Gerratt, and S. Bergbreiter, "First leaps towards jumping microrobots," *IEEE/RSJ International Conference on Intelligent Robots and Systems*, pp. 1680–1686, 2011.

[8] M. Noh, S.-W. Kim, S. An, J.-S. Koh, and K.-J. Cho, "Flea-inspired catapult mechanism for miniature jumping robots," *IEEE Transactions on Robotics*, vol. 28, no. 5, pp. 561–566, 10 2012.

[9] V. Zaitsev, O. Gvirsman, U. B. Hanan, A. Weiss, A. Ayali, and G. Kosa, "A locust-inspired miniature jumping robot," *Bioinspiration Biomimetics*, vol. 10, pp. 1–18, 2015.

[10] D. W. Haldane, M. M. Plecnik, J. K. Yim, and R. S. Fearing, "Robotic vertical jumping agility via series-elastic power modulation," *Science Robotics*, vol. 1, pp. 1–9, 2016.

[11] G.-P. Jung, C. S. Casarez, S.-P. Jung, R. S. Fearing, and K.-J. Cho, "An integrated jumping-crawling robot using height-adjustable jumping module," *IEEE International Conference on Robotics and Automation*, pp. 1–6, 2016.

[12] D. Rus and M. T. Tolley, "Design, fabrication and control of origami robots," *Nature Reviews Materials*, vol. 3, no. 6, p. 101, 2018.

[13] J. P. Whitney, P. S. Sreetharan, K. Y. Ma, and R. J. Wood, "Pop-up book MEMS," *Journal of Micromechanics and Microengineering*, vol. 21, no. 11, p. 115021, 2011.

[14] Z. Zhakypov and J. Paik, "Design methodology for constructing multimaterial origami robots and machines," *IEEE Transactions on Robotics*, vol. 34, no. 1, pp. 1–7, 2 2018.

[15] C. Sung and D. Rus, "Foldable joints for foldable robots," *Journal of Mechanisms and Robotics*, vol. 7, no. 2, p. 021012, 2015.

[16] B. Goldberg, R. Zufferey, N. Doshi, E. F. Helbling, G. Whittredge, M. Kovac, and R. J. Wood, "Power and control autonomy for high-speed locomotion with an insect-scale legged robot," *IEEE Robotics and Automation Letters*, vol. 3, no. 2, pp. 987–993, 2018.

[17] S. Miyashita, S. Guitron, M. Ludersdorfer, C. R. Sung, and D. Rus, "An untethered minature origami robot that self-folds, walks, swims, and degrades," *IEEE International Conference on Robotics and Automation*, pp. 1490–1496, 2015.

[18] C. D. Onal, R. J. Wood, and D. Rus, "An origami-inspired approach to worm robots," *IEEE/ASME Transactions on Mechatronics*, vol. 18, no. 2, pp. 430–438, 2013.

[19] M. Kovac, W. Hraiz, O. Fauria, J.-C. Zufferey, and D. Floreano, "The EPFL jumpglider: A hybrid jumping and gliding robot with rigid or folding wings," *IEEE International Conference on Robotics and Biomimetics*, pp. 1503–1508, 2011.

[20] N. T. Jafferis, E. F. Helbling, M. Karpelson, and R. J. Wood, "Untethered flight of an insect-sized flapping-wing microscale aerial vehicle," *Nature*, vol. 570, no. 7762, p. 491, 2019.

[21] E. D. Demaine and J. O'Rourke, *Geometric Folding Algorithms: Linkages, Origami, Polyhedra*. Cambridge University Press, 2007.

[22] Z. Zhakypov, M. Falahi, M. Shah, and J. Paik, "The design and control of the multi-modal locomotion origami robot, Tribot," *IEEE/RSJ International Conference on Intelligent Robots and Systems*, pp. 4349–4355, 2015.

[23] H. Yuan, J. Pikul, and C. Sung, "Programmable 3-D surfaces using origami tessellations," *7th International Meeting on Origami in Science, Mathematics, and Education*, pp. 893–906, 2018.

[24] W.-H. Chen, S. Misra, Y. Gao, Y.-J. Lee, D. E. Koditschek, S. Yang, and C. R. Sung, "A programmably compliant origami mechanism for dynamically dexterous robots," *IEEE Robotics and Automation Letters*, vol. 5, pp. 2131–2137, 2020.

[25] N. P. Bende, T. Yu, N. A. Corbin, M. A. Dias, C. D. Santangelo, J. A. Hanna, and R. C. Hayward, "Overcurvature induced multistability of linked conical frustra: how a "bendy straw" holds its shape," *Soft Matter*, vol. 14, pp. 8636–8642, 2018.

[26] L. L. Howell, "Compliant mechanisms," *21st Century Kinematics*, pp. 189–216, 2013.

[27] B. D. Jensen and L. L. Howell, "Bistable configurations of compliant mechanisms modeled using four links and translational joints," *Journal of Mechanical Design*, pp. 657–666, 2004.